Supporting Information

Revealing the direct role of cobalt in oxygen evolution reaction initiation for high-performance iridium-cobalt oxide catalysts

Qianyu Lin[a,#], Qintao Sun[a,#], Haojie Xu[a], Feiyang Yu[c], Wenwen Li[a], Haizhou Yu[a], Mingwang Shao[a], Hui Huang[a], Zhenglong Fan[a,*], Tao Cheng[a,*], Fan Liao[a,*], Yang Liu[a,*] and Zhenhui Kang[a,b,*]

[a] State Key Laboratory of Bioinspired Interfacial Materials Science, Institute of Functional Nano & Soft Materials (FUNSOM), Soochow University, 199 Ren'ai Road, Suzhou, 215123, Jiangsu, PR China.

[b] Macao Institute of Materials Science and Engineering (MIMSE), MUST-SUDA Joint Research Center for Advanced Functional Materials, Macau University of Science and Technology, Taipa 999078, Macao, China.

[c] Key Laboratory of Polyoxometalate and Reticular Material Chemistry of Ministry of Education, Northeast Normal University, Changchun, 130024, China.

* Correspondence to: zlfan@suda.edu.cn (ZL Fan); tcheng@suda.edu.cn (T Cheng); fliao@suda.edu.cn (F Liao); yangl@suda.edu.cn (Y Liu); zhkang@suda.edu.cn (ZH Kang).

[#] Q. Y. Lin and Q. T. Sun contributed equally to this work.

Supplementary Text

1. Experimental section

1.1. Structure Characterization

The phase and crystallographic information of the samples were analyzed by XRD using a Philips X'pert PRO MPD diffractometer with Cu Kα radiation (λ = 0.15406 nm). TEM observations and EDX elemental mapping were carried out on a Talos F200X operated at 200 kV. STEM imaging was performed on a JEOL ARM200CF operated at 80 kV, and selected images were refined with a Gaussian filter to enhance contrast. SEM measurements were obtained using a SU8230 field-emission microscope at 10 kV. Prior to TEM and STEM analysis, the samples were baked at 140 °C for 8 h to minimize surface moisture. XPS was conducted on a Kratos AXIS UltraDLD system with Al Kα excitation (1486 eV) to examine the surface chemical states. XAS measurements were collected at the 14 W beamline of the Shanghai Synchrotron Radiation Facility. The elemental composition of the products was quantified by ICP-MS (Analytikjena M90).

1.2. Electrochemical Measurements

All OER measurements were performed at room temperature on a CHI 760D electrochemical workstation using a single-compartment three-electrode configuration. A glassy carbon electrode (GCE, 3 mm) coated with catalyst ink served as the working electrode, with an SCE as the reference and a Pt wire as the counter electrode. The catalyst ink was obtained by dispersing 4 mg of sample ($Ir_{0.3}Co_{0.7}O_x$, Com.IrO_2, CoO_x and Co_3O_4) in a mixture of 900 μL isopropanol and 100 μL Nafion solution (0.5 wt%), followed by ultrasonication to ensure uniformity. A 5 μL aliquot of the ink was dropped onto the GCE

and dried before use. All potentials were converted to the RHE scale in acidic media using E (vs. RHE) = E (vs.Hg/$HgCl_2$) + 0.244 V + pH*0.0591 V. OER testing was conducted in O_2-saturated 0.5 M H_2SO_4 with 95% i*R* compensation while continuously stirring the electrolyte. LSV was recorded from 1.2 to 1.8 V (vs. RHE) at 5 mV s^{-1}. The SCE was calibrated in 0.5 M H_2SO_4 using a Pt electrode at 1 mV s^{-1}.

Catalyst durability was assessed by chronopotentiometry at a constant geometric current density of 10 mA cm^{-2}. For stability evaluation, 200 μL of the catalyst dispersion (4 mg mL^{-1}) was deposited on carbon paper (0.5 cm × 0.5 cm) and dried. During long-term operation, the electrolyte (50 mL total) was periodically sampled (5 mL each time) for ICP-MS analysis; an equal volume of fresh 0.5 M H_2SO_4 was replenished after each sampling to maintain constant volume. EIS spectra were collected between 10^5 and 10^{-1} Hz.

The double-layer capacitance (Cdl) was determined from CV curves acquired at scan rates between 10 and 60 mV s^{-1}. Cdl was obtained from the slope of Δj/2 versus v according to:

$$C_{dl} = \frac{\Delta j/2}{v}$$

The ECSA is estimated from the C_{dl} of the catalytic surface and can be quantified according to the following equation:

$$ECSA = \frac{C_{dl}}{C_s}$$

1.3. TPS Measurements

The TPS measurements were carried out on a homemade measuring apparatus. A 470 µF capacitor with an adjustable voltage to charge it is part of the circuit. The working electrode (GCE) is connected to the

positive electrode, and the reference electrode (SCE) and counter electrode (carbon rod) are connected to the negative electrode. O_2-saturated 0.5 M H_2SO_4 was used as electrolyte. 2 μL of the catalyst solution was loaded on the surface of GCE and dried naturally for testing. Potential and current values were recorded at a data acquisition rate of 100,000 samples per second.

1.4. DFT calculations

The ab initio quantum mechanical (QM) calculations were carried out using VASP (version 5.4.4) with the projector augmented wave (PAW) method and a plane-wave basis set. Density functional theory (DFT) was employed with the Perdew–Burke–Ernzerhof (PBE) generalized gradient approximation[1]. Dispersion interactions were treated using the DFT-D3 scheme with Becke–Jonson damping[2]. An energy cut-off of 400 eV was used, as higher cut-off values did not improve the accuracy in our benchmark tests. Brillouin-zone sampling was performed using a Γ-centered Monkhorst–Pack mesh of 3×3×1, and finer k-point spacing did not lead to noticeable gains in predictive accuracy. Partial occupancies were described using the first-order Methfessel–Paxton smearing method with a width of 0.05 eV. Electronic self-consistency was reached when both the total energy variation and the change in eigenvalues between successive steps were below 1×10^{-5} eV.

1.5. Universal machine learning force field

The universal machine learning force field used in this work is built on the equivariant graph neural network framework NequIP, referred to as SevenNet, which spans most elements in the periodic table and is tailored for inorganic crystalline systems[3]. All structure optimizations and molecular dynamics (MD) simulations with this force field were carried out through the Atomic Simulation Environment

(ASE)[4,5]. Geometry relaxations employed the limited-memory BFGS algorithm[6], with both atomic positions and cell parameters adjusted simultaneously until the residual forces were below 0.02 eV $Å^{-1}$. For MD simulations, the stability of $Ir_{0.3}Co_{0.7}O_x$ was assessed under a canonical (NVT) ensemble, using a time step of 1 fs.

2. Supplementary Figures

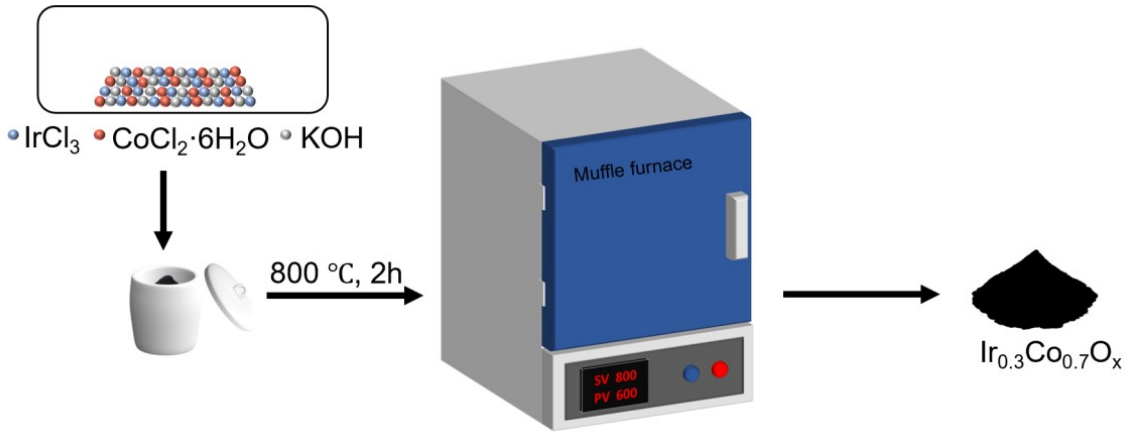

Fig. S1. Synthesis of $Ir_{0.3}Co_{0.7}O_x$ *via* the molten-alkali synthesis strategy.

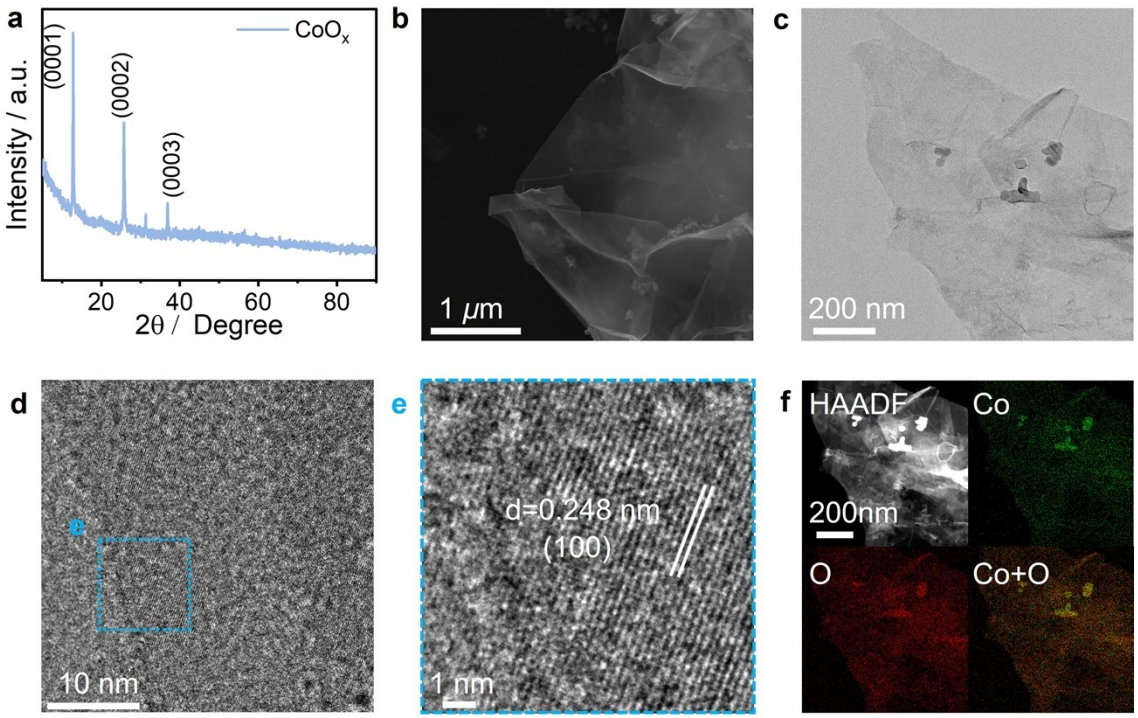

Fig. S2. (a) XRD pattern of CoO_x. (b) SEM image, (c) TEM image of CoO_x. (d) HRTEM image of CoO_x and (e) its partial enlargement. (f) HAADF-STEM image and corresponding EDX mapping of CoO_x.

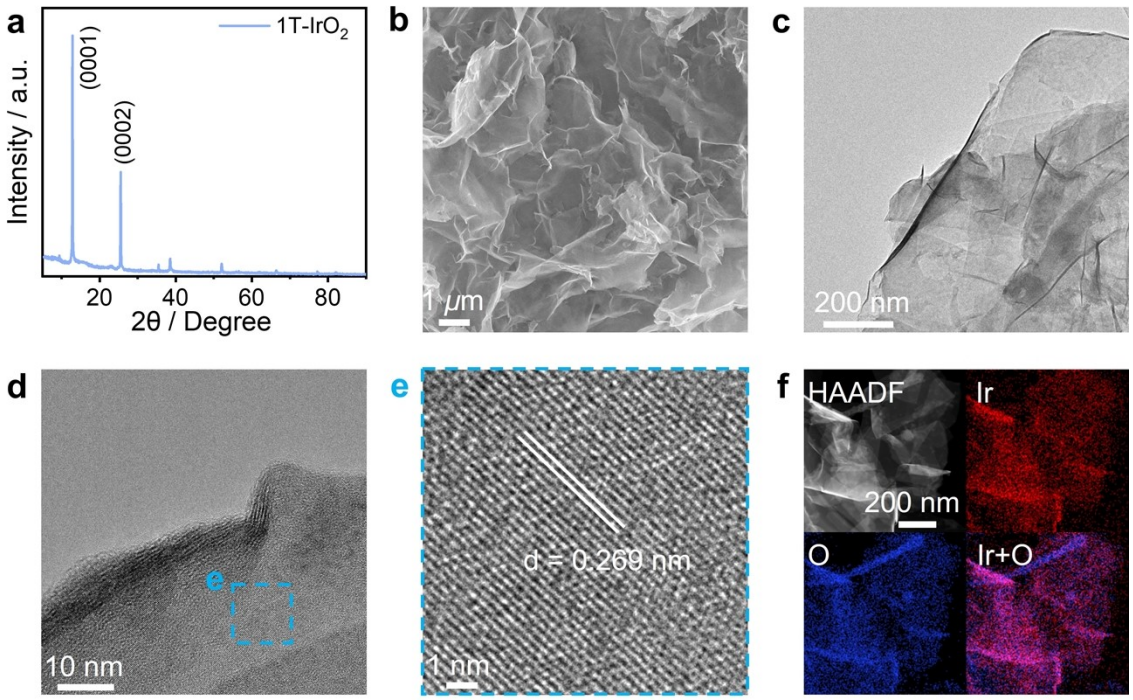

Fig. S3. (a) XRD pattern of 1T-IrO_2. (b) SEM image, (c) TEM image of 1T-IrO_2. (d) HRTEM image of 1T-IrO_2 and (e) its partial enlargement. (f) HAADF-STEM image and corresponding EDX mapping of 1T-IrO_2.

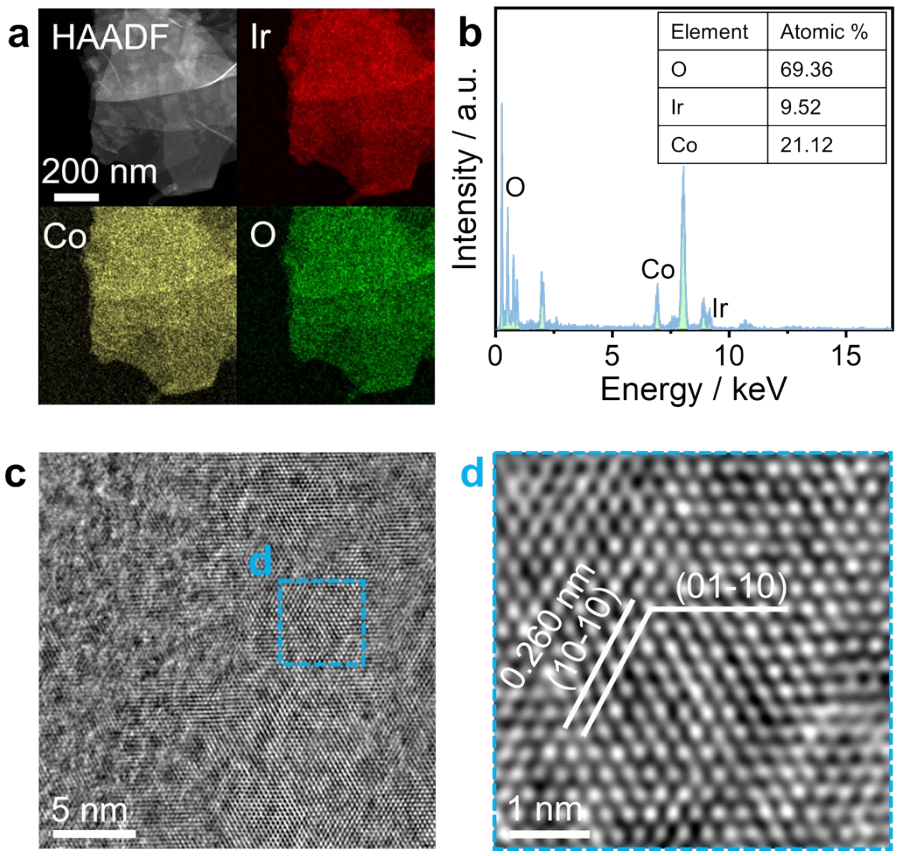

Fig. S4. (a) HAADF-STEM image and corresponding EDX mapping of $Ir_{0.3}Co_{0.7}O_x$. (b) TEM-EDX spectrum of $Ir_{0.3}Co_{0.7}O_x$. (c) HRTEM image of $Ir_{0.3}Co_{0.7}O_x$ and (d) its partial enlargement.

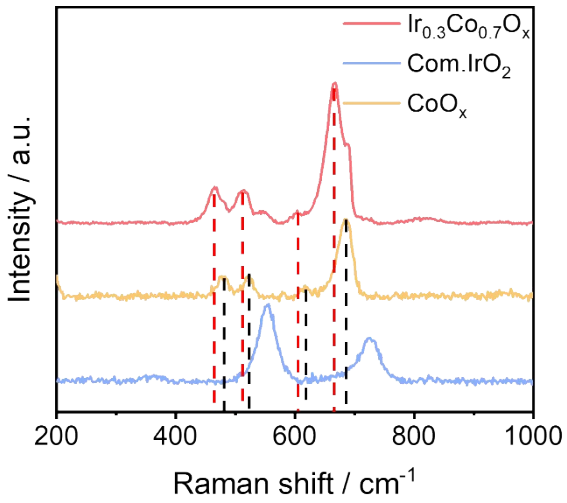

Fig. S5. Raman spectra of $Ir_{0.3}Co_{0.7}O_x$, Com.IrO_2 and CoO_x.

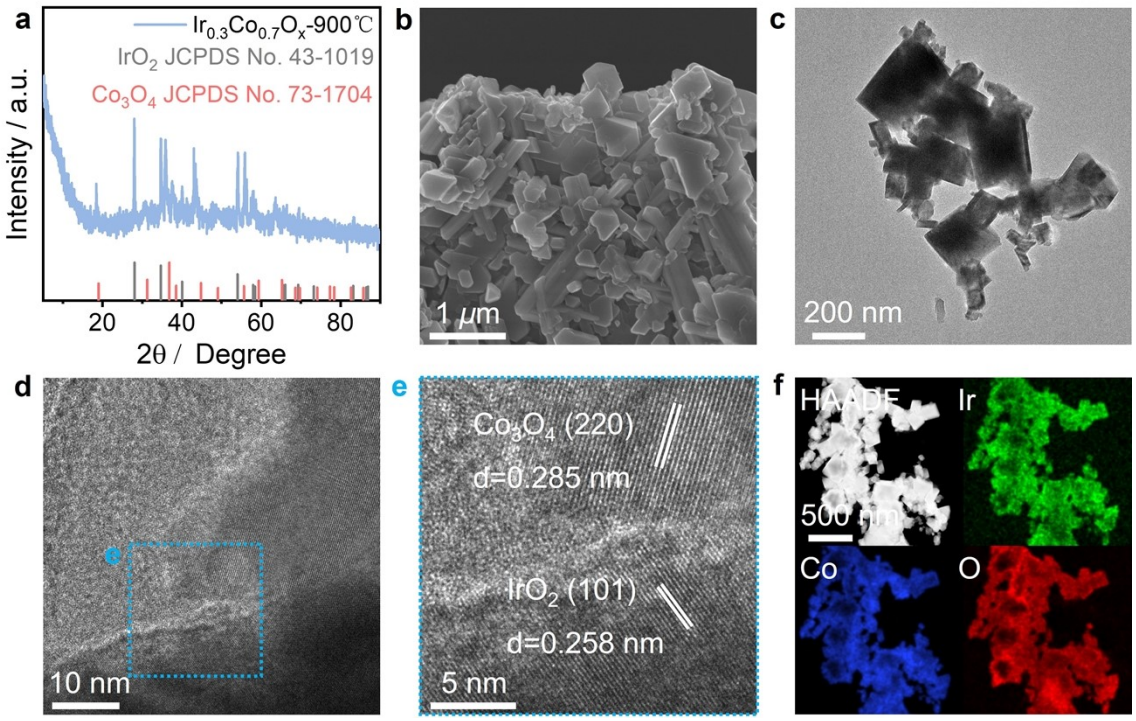

Fig. S6. (a) XRD pattern of $Ir_{0.3}Co_{0.7}O_x$-900 °C. (b) SEM image, (c) TEM image of $Ir_{0.3}Co_{0.7}O_x$-900 °C. (d) HRTEM image of $Ir_{0.3}Co_{0.7}O_x$-900 °C and (e) its partial enlargement. (f) HAADF-STEM image and corresponding EDX mapping of $Ir_{0.3}Co_{0.7}O_x$-900 °C.

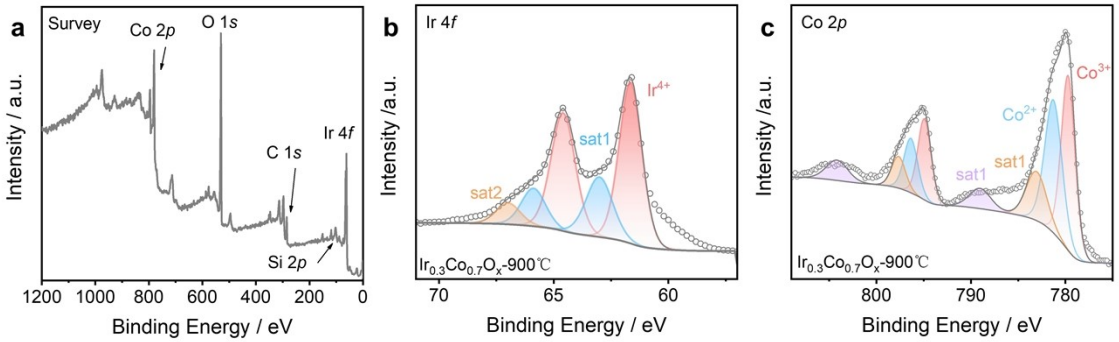

Fig. S7. (a) Full-scan, (b) Ir 4*f* and (c) Co 2*p* XPS spectra of $Ir_{0.3}Co_{0.7}O_x$-900 °C.

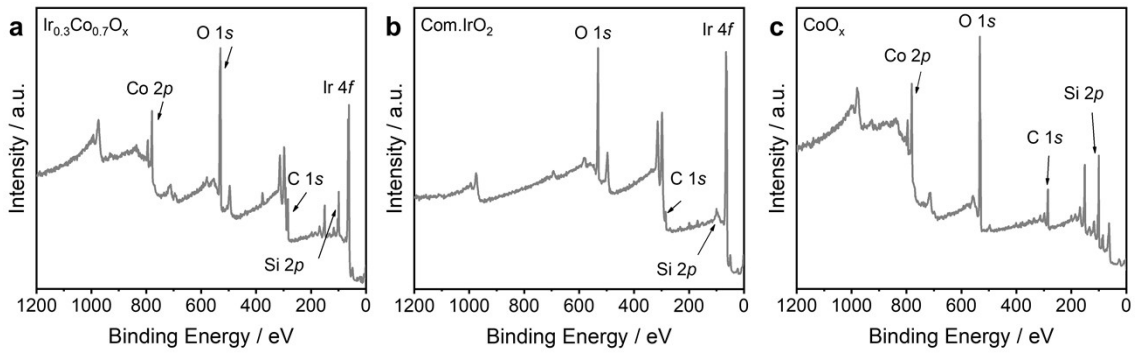

Fig. S8. Full-scan XPS spectra of $Ir_{0.3}Co_{0.7}O_x$, $Com.IrO_2$ and CoO_x.

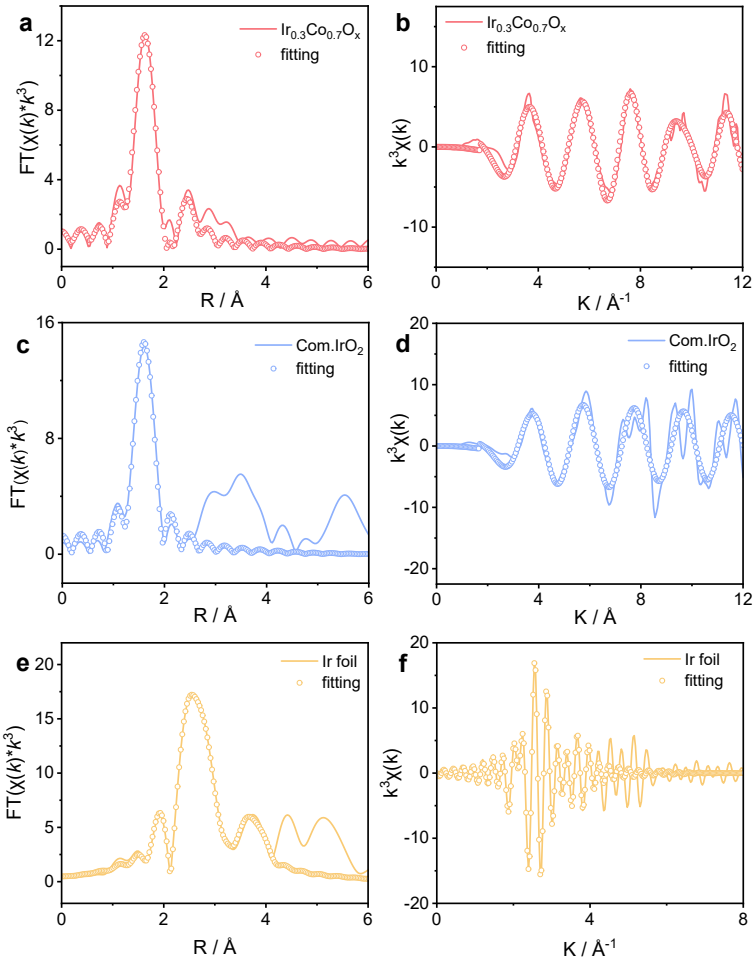

Fig. S9. R space fitting results of Ir L_3-edge for (a) $Ir_{0.3}Co_{0.7}O_x$, (c) Com.IrO_2 and (e) Ir foil. Inverse FT-EXAFS fitting results of Ir L_3-edge for (b) $Ir_{0.3}Co_{0.7}O_x$, (d) Com.IrO_2 and (f) Ir foil.

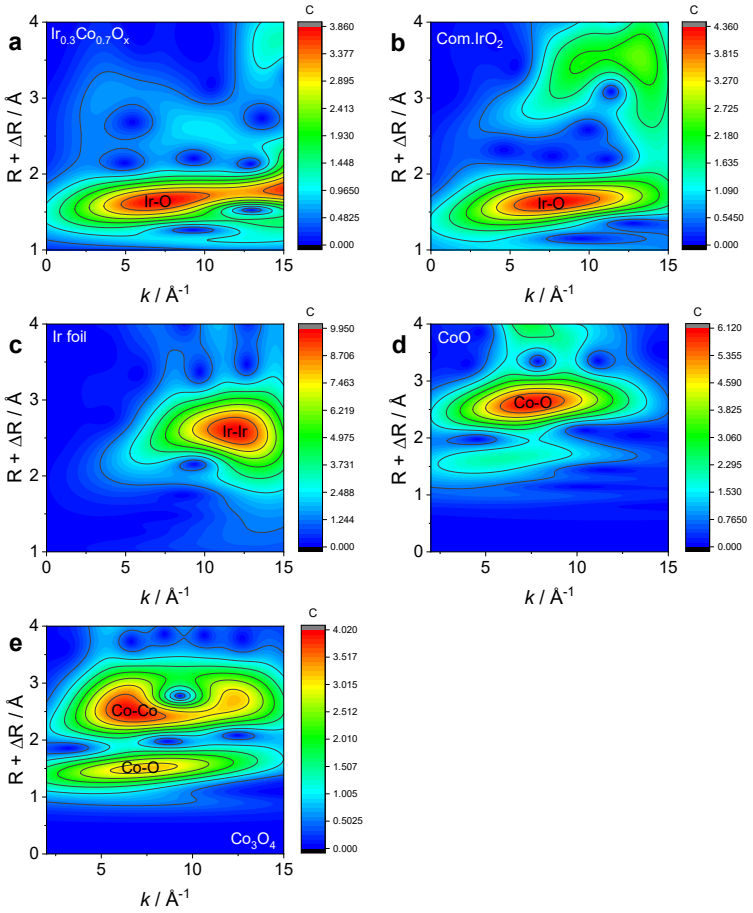

Fig. S10. Ir L_3-edge WT-EXAFS of (a) $Ir_{0.3}Co_{0.7}O_x$, (b) Com.IrO_2 and (c) Ir foil. Co K-edge WT-EXAFS of (d) CoO and (e) Co_3O_4.

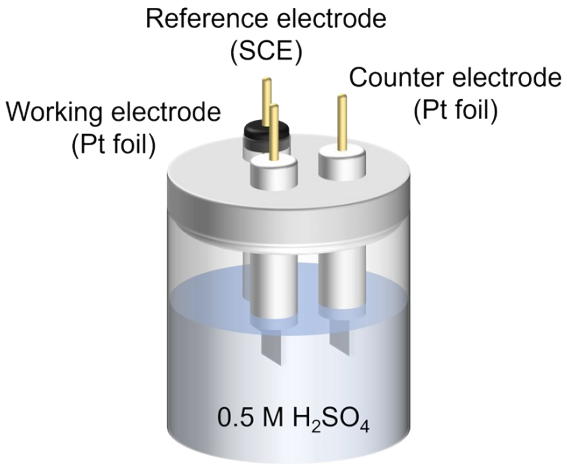

Fig. S11. Schematic diagram of the calibration reference electrode (SCE), using Pt foils as the working and counter electrodes.

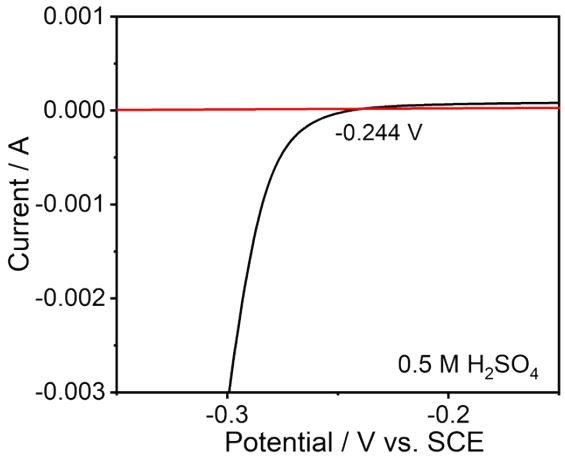

Fig. S12. Calibration of SCE in 0.5 M H_2SO_4 electrolyte.

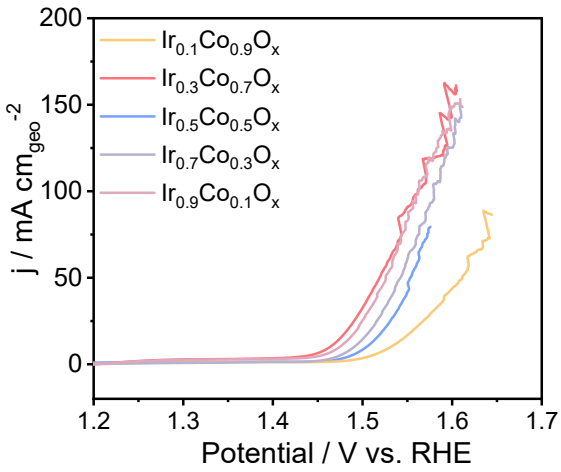

Fig. S13. The OER polarization curves of $Ir_{0.1}Co_{0.9}O_x$, $Ir_{0.3}Co_{0.7}O_x$, $Ir_{0.5}Co_{0.5}O_x$, $Ir_{0.7}Co_{0.3}O_x$ and $Ir_{0.9}Co_{0.1}O_x$ without iR correction.

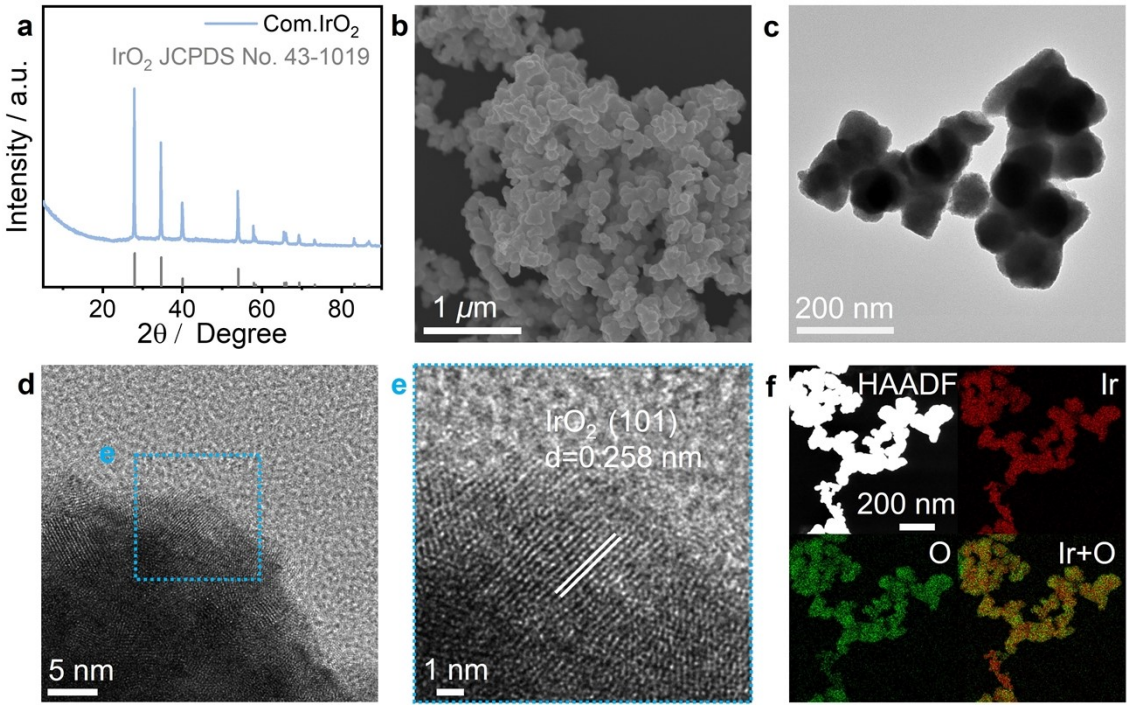

Fig. S14. (a) XRD pattern of Com.IrO_2. (b) SEM image, (c) TEM image of Com.IrO_2. (d) HRTEM image of Com.IrO_2 and (e) its partial enlargement. (f) HAADF-STEM image and corresponding EDX mapping of Com.IrO_2.

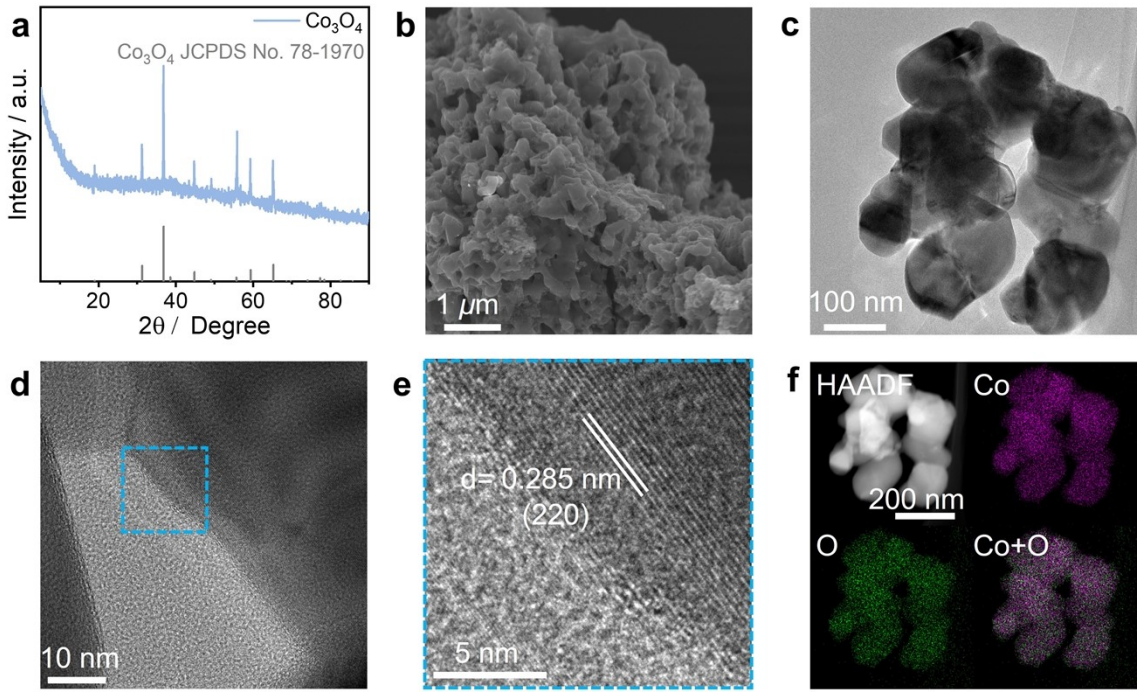

Fig. S15. (a) XRD pattern of Co_3O_4. (b) SEM image, (c) TEM image of Co_3O_4. (d) HRTEM image of Co_3O_4 and (e) its partial enlargement. (f) HAADF-STEM image and corresponding EDX mapping of of Co_3O_4.

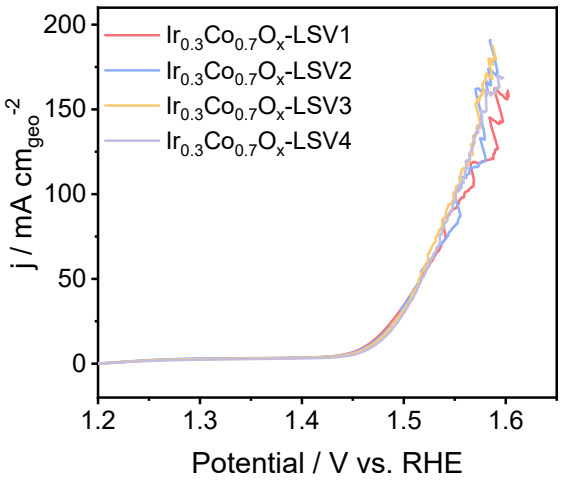

Fig. S16. Reproducibility of LSV scans for $Ir_{0.3}Co_{0.7}O_x$ catalyst without iR correction.

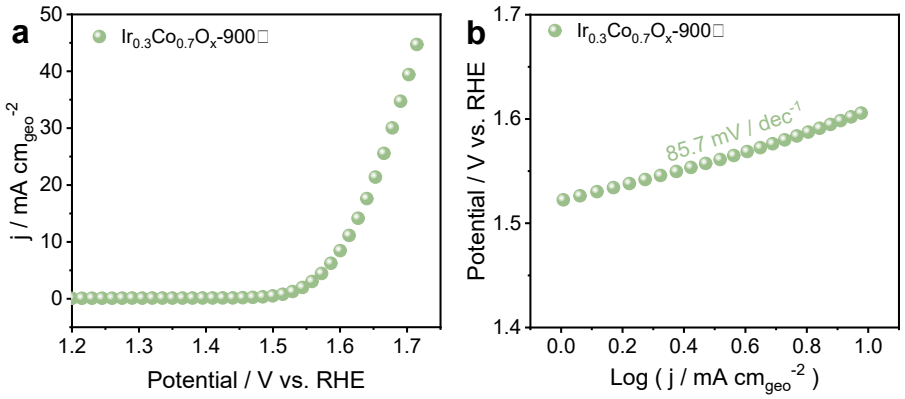

Fig. S17. (a) The OER polarization curves of $Ir_{0.3}Co_{0.7}O_x$-900 ℃ without iR correction. (b) Tafel plots obtained from the polarization curves of $Ir_{0.3}Co_{0.7}O_x$-900 ℃ in Fig. S 16a.

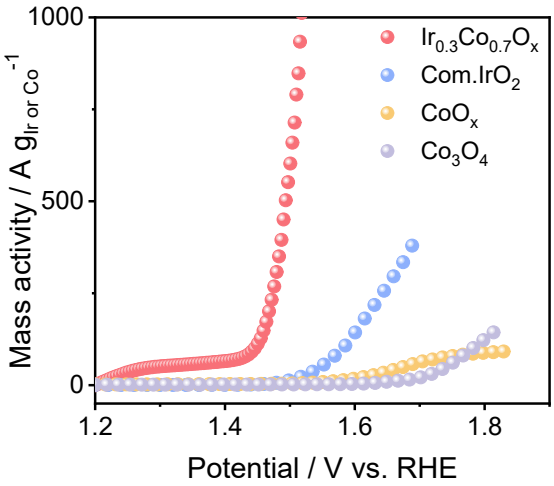

Fig. S18. Mass activities for $Ir_{0.3}Co_{0.7}O_x$, $Com.IrO_2$, CoO_x and Co_3O_4.

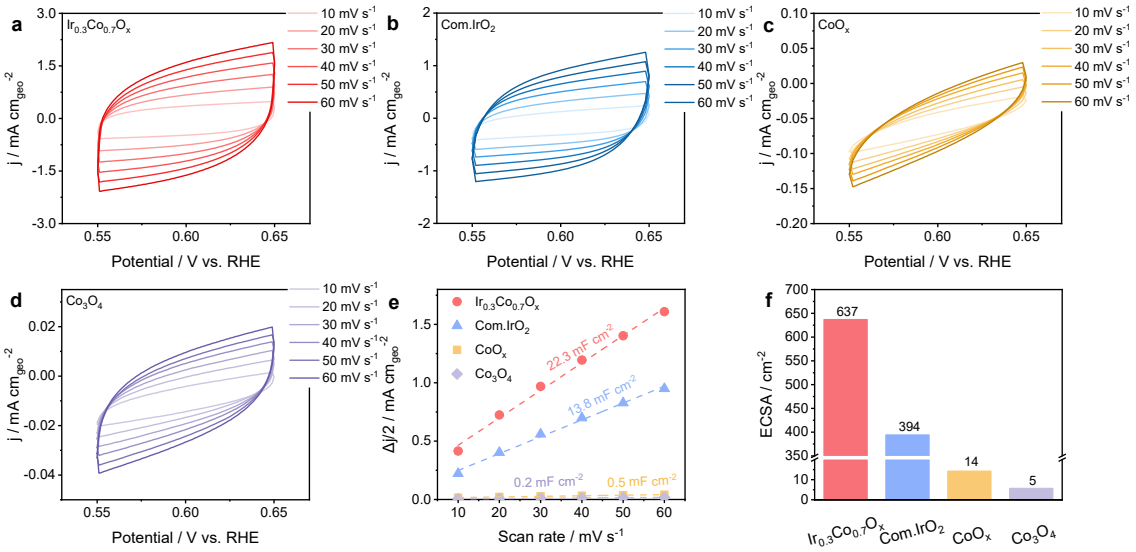

Fig. S19. CV curves of (a) $Ir_{0.3}Co_{0.7}O_x$, (b) $Com.IrO_2$, (c) CoO_x and (d) Co_3O_4 in the double-layer region. (e) Plots of the charging current density as functions of the scan rate of $Ir_{0.3}Co_{0.7}O_x$, $Com.IrO_2$, CoO_x and Co_3O_4. (f) The comparison of ECSA values.

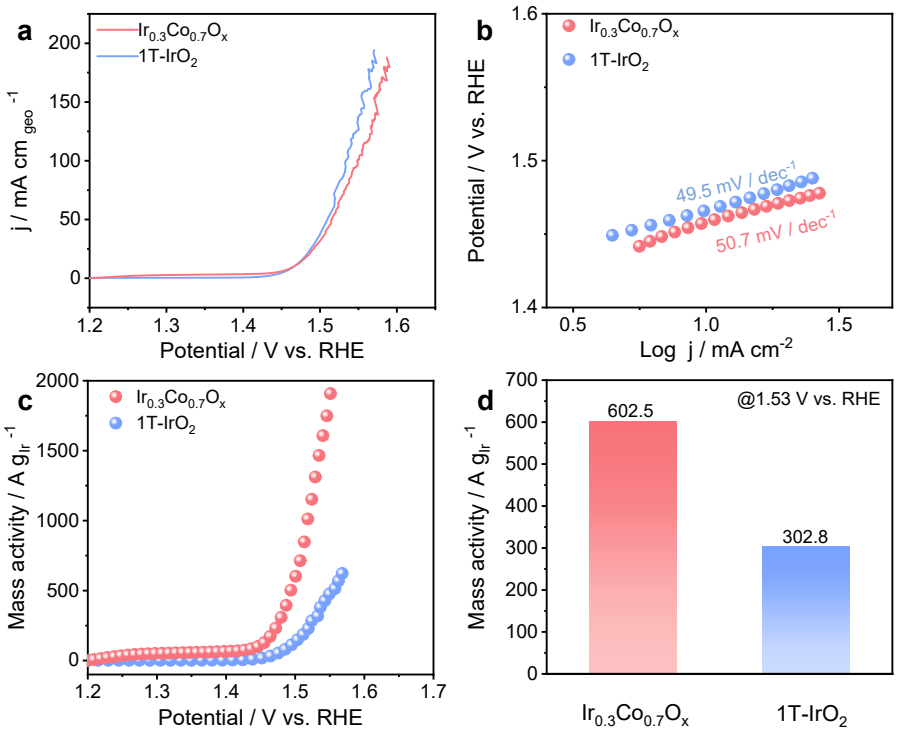

Fig. S20. (a) The OER polarization curves of $Ir_{0.3}Co_{0.7}O_x$ and 1T-IrO_2. (b) Tafel plots obtained from the polarization curves of $Ir_{0.3}Co_{0.7}O_x$ and 1T-IrO_2 in Fig. S 19a. (c) Mass activities for $Ir_{0.3}Co_{0.7}O_x$ and 1T-IrO_2. (d) Comparison of the mass activities at 1.53 V vs. RHE for $Ir_{0.3}Co_{0.7}O_x$ and 1T-IrO_2.

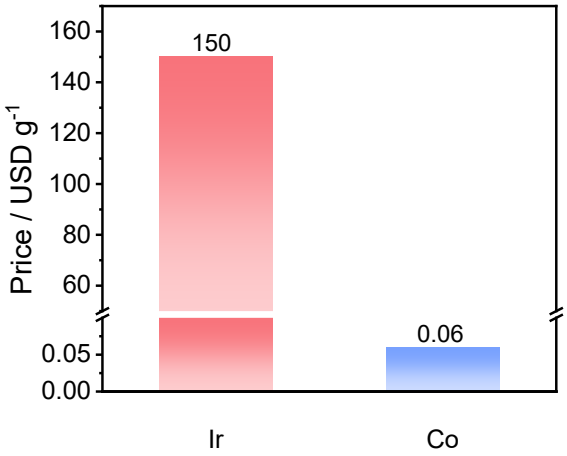

Fig. S21. Iridium and cobalt price comparison.

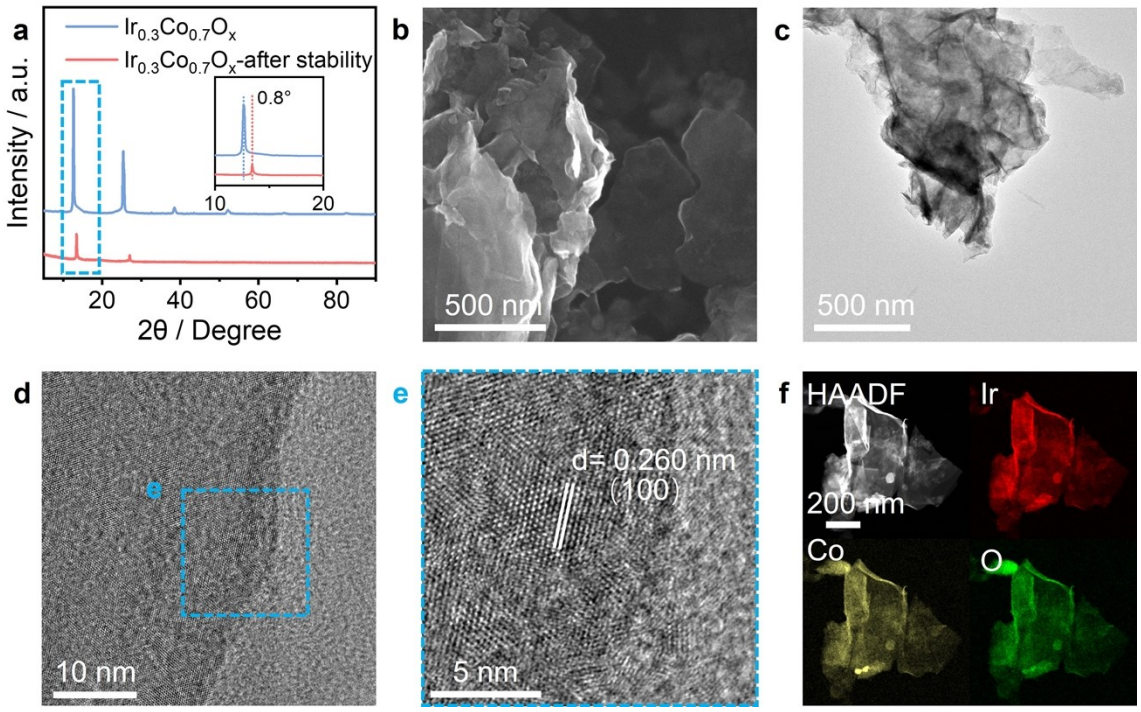

Fig. S22. (a) XRD patterns of $Ir_{0.3}Co_{0.7}O_x$ before and after long-term stability test. (b) SEM image, (c) TEM image of $Ir_{0.3}Co_{0.7}O_x$ after long-term stability test. (d) HRTEM image of $Ir_{0.3}Co_{0.7}O_x$ after long-term stability test and (e) its partial enlargement. (f) HAADF-STEM image and corresponding EDX mapping of $Ir_{0.3}Co_{0.7}O_x$ after long-term stability test.

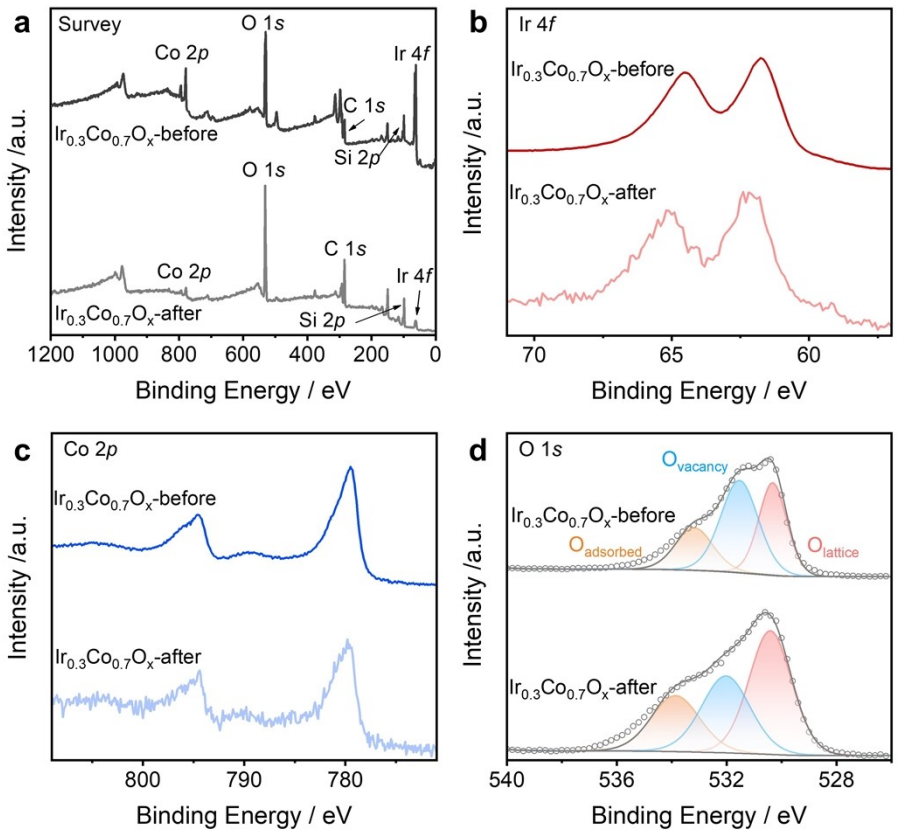

Fig. S23. (a) Full scan, (b) Ir 4*f*, (c) Co 2*p* and (d) O 1*s* XPS spectra of $Ir_{0.3}Co_{0.7}O_x$ before and after stability test.

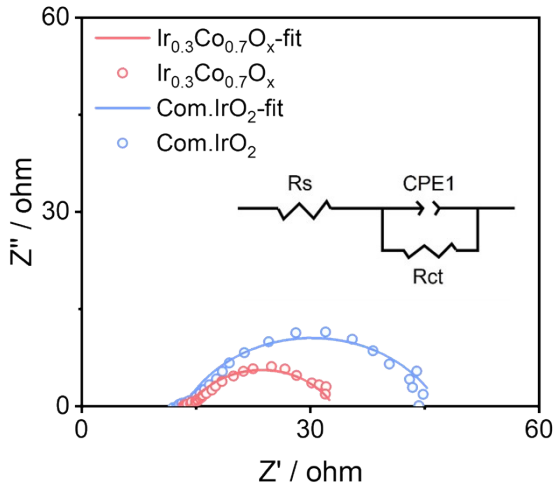

Fig. S24. EIS of $Ir_{0.3}Co_{0.7}O_x$ and $Com.IrO_2$. The Rct values for $Ir_{0.3}Co_{0.7}O_x$ and $Com.IrO_2$ were 18.93 and 33.5 Ω, respectively.

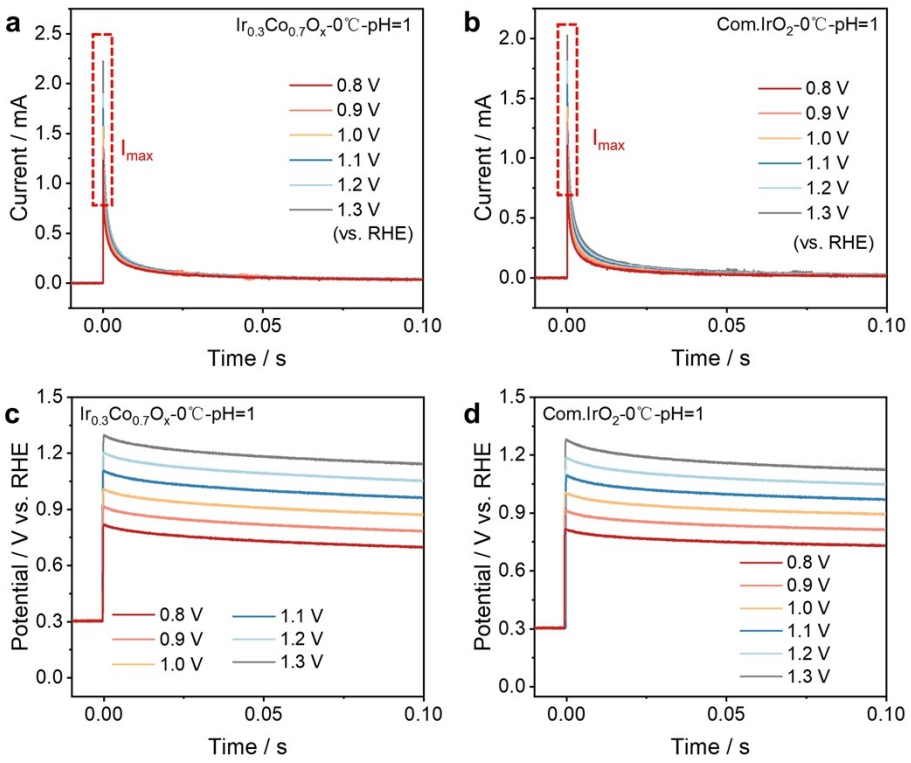

Fig. S25. (a-b) Current decay curves of $Ir_{0.3}Co_{0.7}O_x$ and Com.IrO_2 under different voltages at 0°C and pH = 1. (c-d) Curves of actual voltages of $Ir_{0.3}Co_{0.7}O_x$ and Com.IrO_2 over time at 0°C and pH = 1.

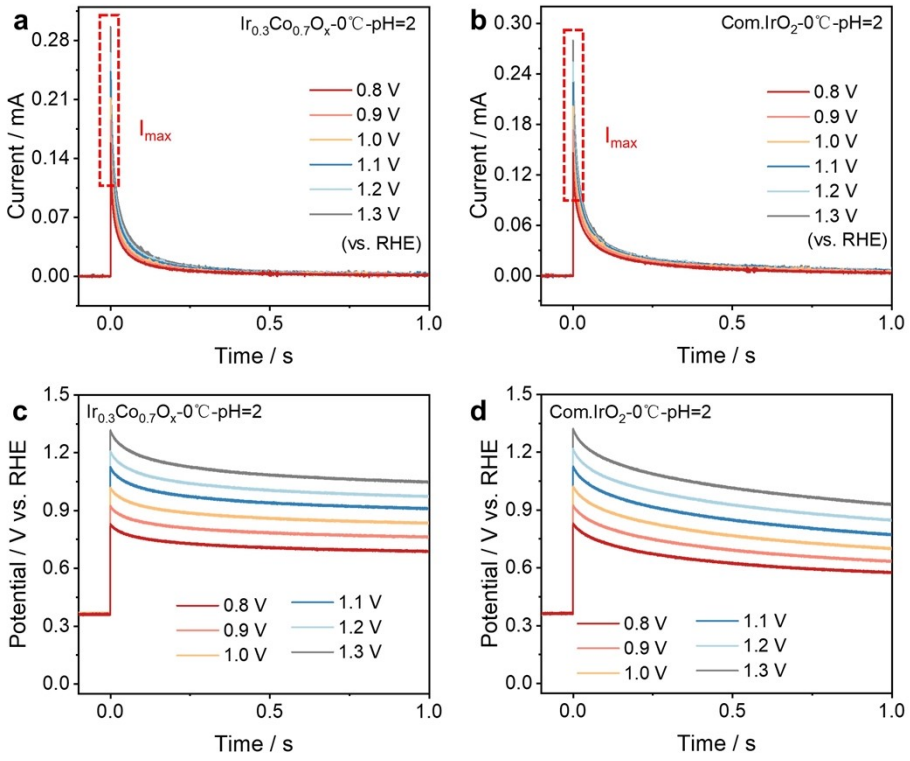

Fig. S26. (a-b) Current decay curves of $Ir_{0.3}Co_{0.7}O_x$ and Com.IrO_2 under different voltages at 0°C and pH = 2. (c-d) Curves of actual voltages of $Ir_{0.3}Co_{0.7}O_x$ and Com.IrO_2 over time at 0°C and pH = 2.

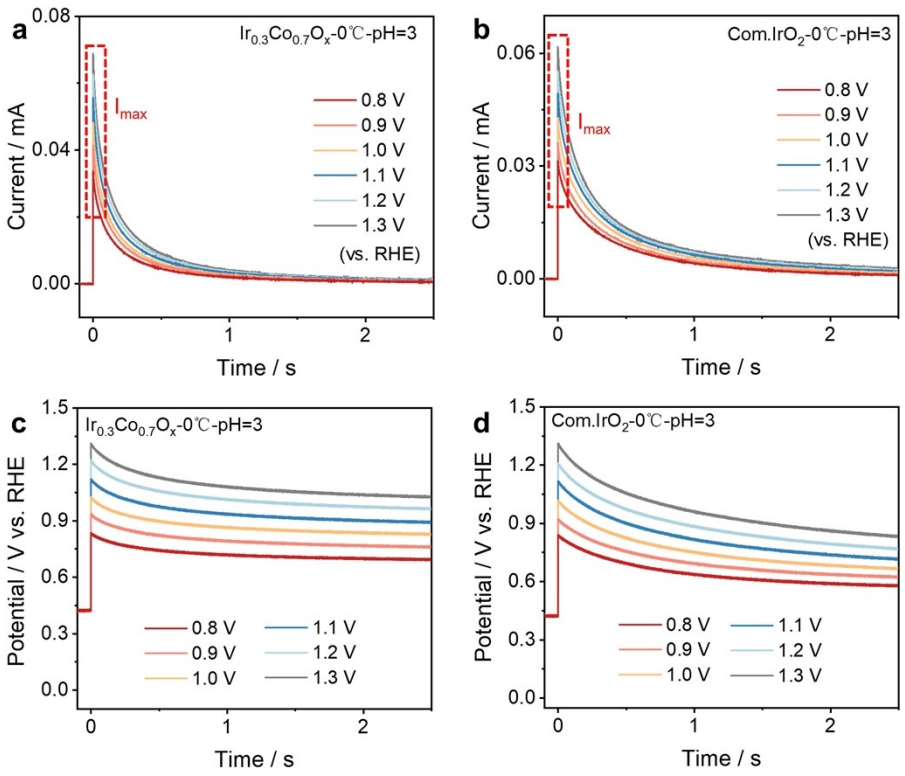

Fig. S27. (a-b) Current decay curves of $Ir_{0.3}Co_{0.7}O_x$ and Com.IrO_2 under different voltages at 0°C and pH = 3. (c-d) Curves of actual voltages of $Ir_{0.3}Co_{0.7}O_x$ and Com.IrO_2 over time at 0°C and pH = 3.

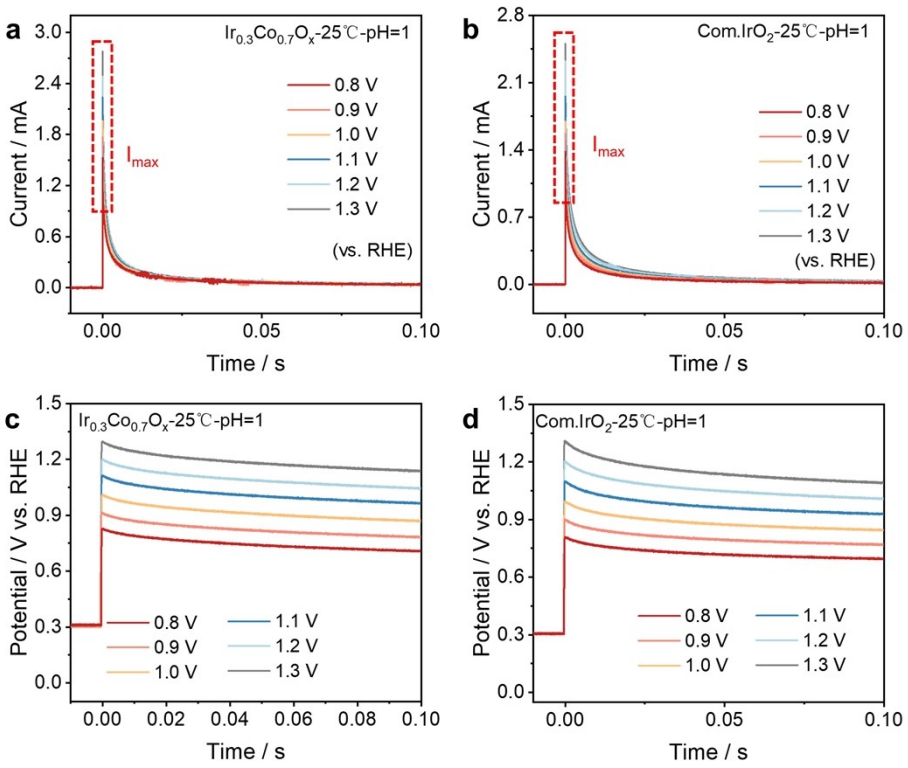

Fig. S28. (a-b) Current decay curves of $Ir_{0.3}Co_{0.7}O_x$ and Com.IrO_2 under different voltages at 25°C and pH = 1. (c-d) Curves of actual voltages of $Ir_{0.3}Co_{0.7}O_x$ and Com.IrO_2 over time at 25°C and pH = 1.

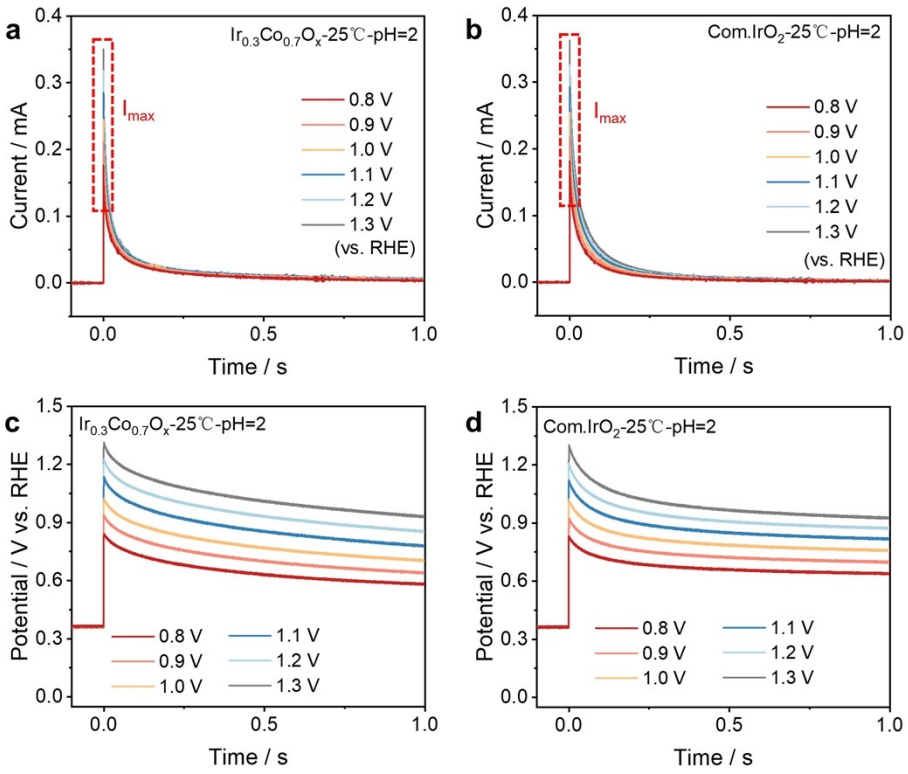

Fig. S29. (a-b) Current decay curves of $Ir_{0.3}Co_{0.7}O_x$ and Com.IrO_2 under different voltages at 25°C and pH = 2. (c-d) Curves of actual voltages of $Ir_{0.3}Co_{0.7}O_x$ and Com.IrO_2 over time at 25°C and pH = 2.

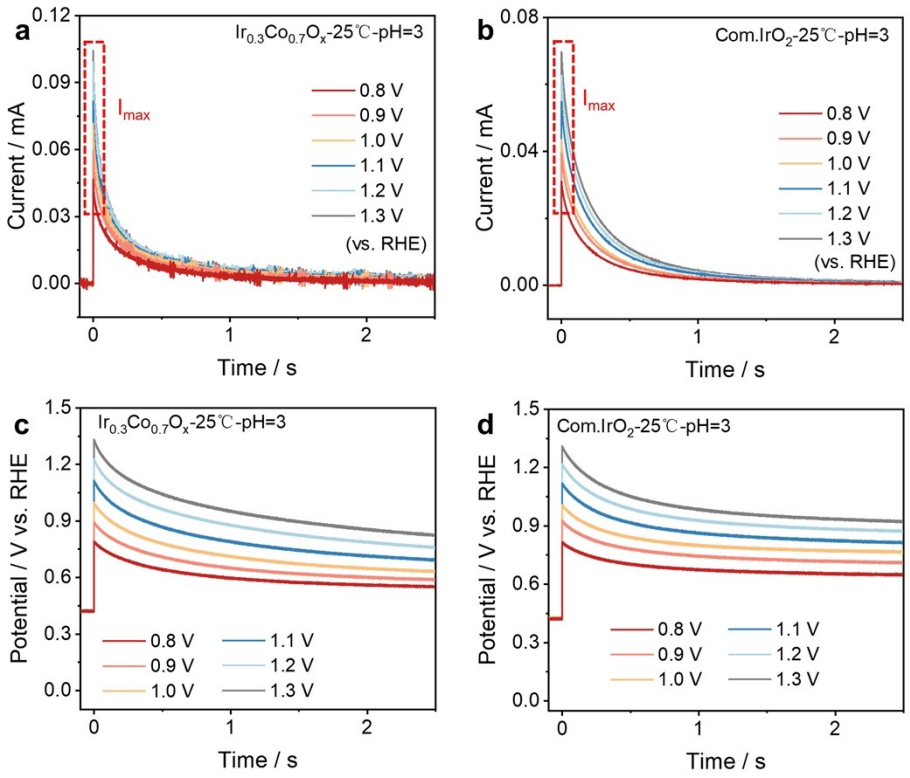

Fig. S30. (a-b) Current decay curves of $Ir_{0.3}Co_{0.7}O_x$ and Com.IrO_2 under different voltages at 25°C and pH = 3. (c-d) Curves of actual voltages of $Ir_{0.3}Co_{0.7}O_x$ and Com.IrO_2 over time at 25°C and pH = 3.

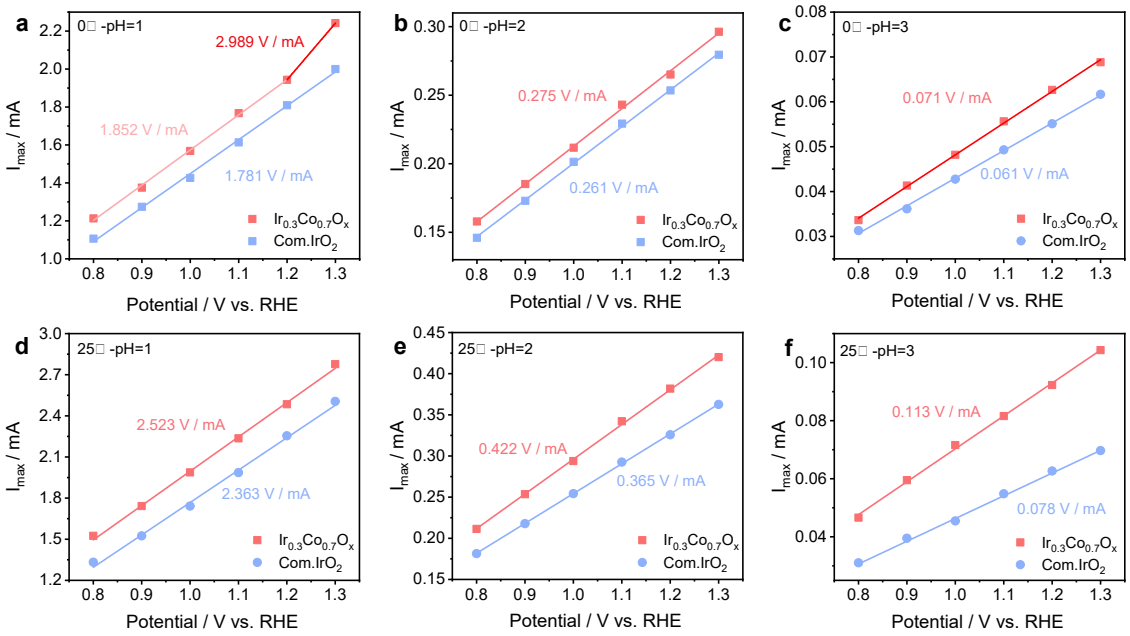

Fig. S31. (a) The peak currents $Ir_{0.3}Co_{0.7}O_x$ and $Com.IrO_2$ under different voltages at 0°C and pH = 1. (b) The peak currents $Ir_{0.3}Co_{0.7}O_x$ and $Com.IrO_2$ under different voltages at 0°C and pH = 2. (c) The peak currents $Ir_{0.3}Co_{0.7}O_x$ and $Com.IrO_2$ under different voltages at 0°C and pH = 3. (d) The peak currents $Ir_{0.3}Co_{0.7}O_x$ and $Com.IrO_2$ under different voltages at 25°C and pH = 1. (e) The peak currents $Ir_{0.3}Co_{0.7}O_x$ and $Com.IrO_2$ under different voltages at 25°C and pH = 2. (f) The peak currents $Ir_{0.3}Co_{0.7}O_x$ and $Com.IrO_2$ under different voltages at 25°C and pH = 3.

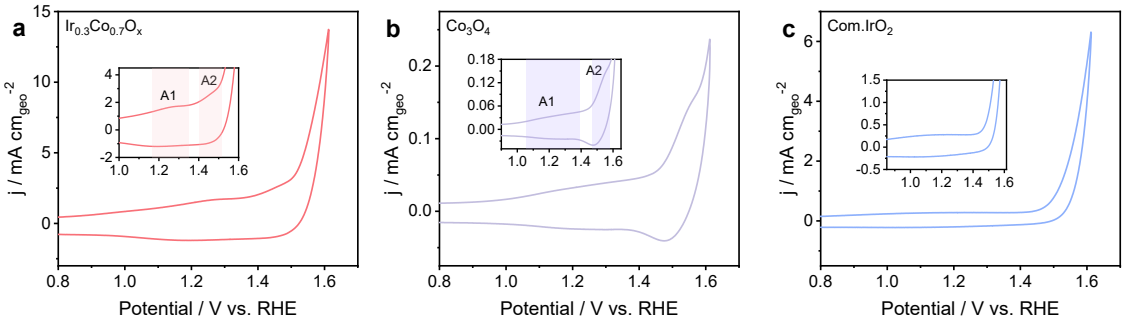

Fig. S32. CV curves of (a) $Ir_{0.3}Co_{0.7}O_x$, (b) Com.IrO_2 and (c) CoO_x in 1 M Na_2SO_4.

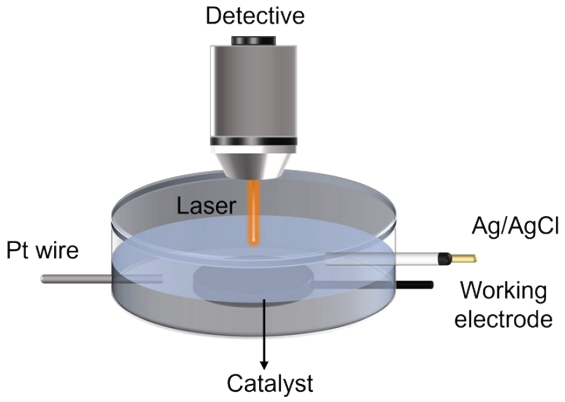

Fig. S33. Schematic illustration of the *in-situ* Raman measurements.

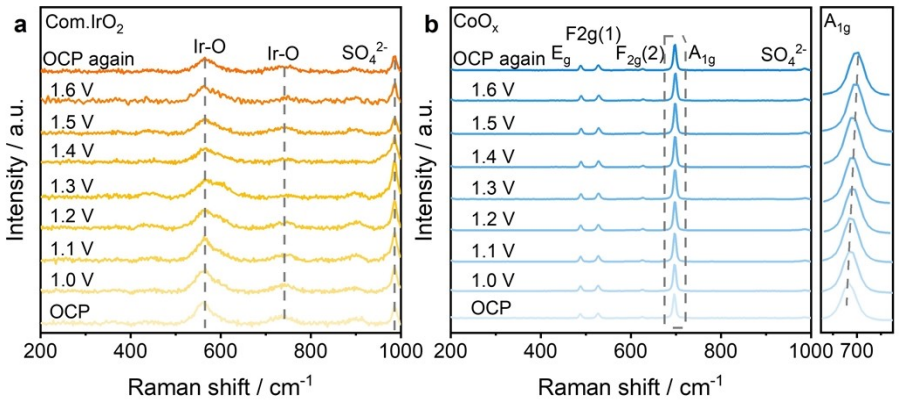

Fig. S34. *In-situ* Raman spectra of (a) Com.IrO_2 and (b) CoO_x electrocatalysts in O_2-saturated 0.5 M H_2SO_4.

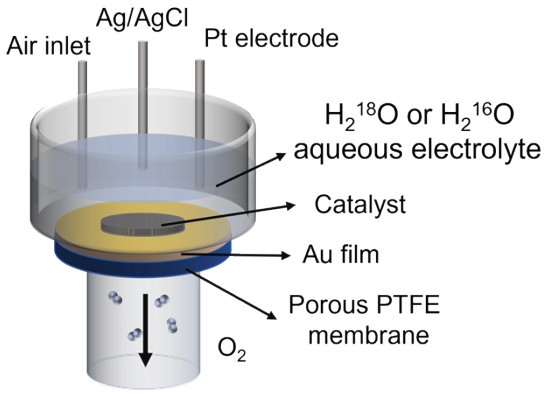

Fig. S35. Schematic illustration of the *in-situ* ^{18}O-labeled DEMS measurements.

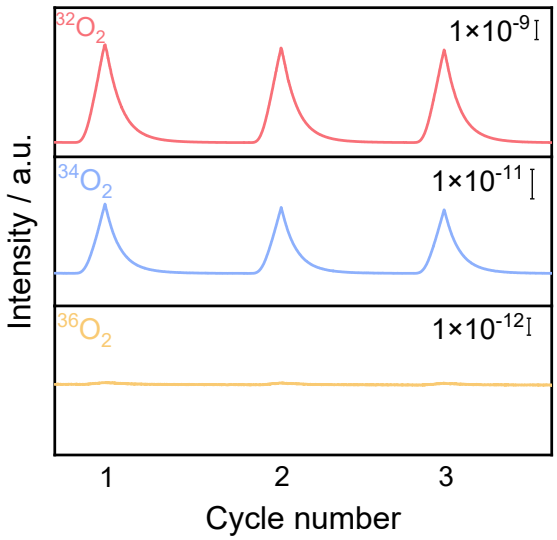

Fig. S36. *In-situ* ^{18}O-labeled DEMS background signals for $^{32}O_2$ ($^{16}O^{16}O$), $^{34}O_2$ ($^{16}O^{18}O$), and $^{36}O_2$ ($^{18}O^{18}O$) from the reaction products of $Ir_{0.3}Co_{0.7}O_x$ catalysts in $H_2{}^{16}O$ (0.5 M H_2SO_4 electrolyte).

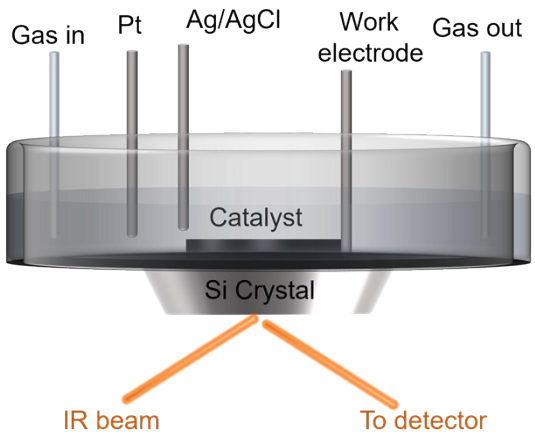

Fig. S37. Schematic illustration of the custom-designed cell for *in-situ* ATR-SEIRAS measurements.

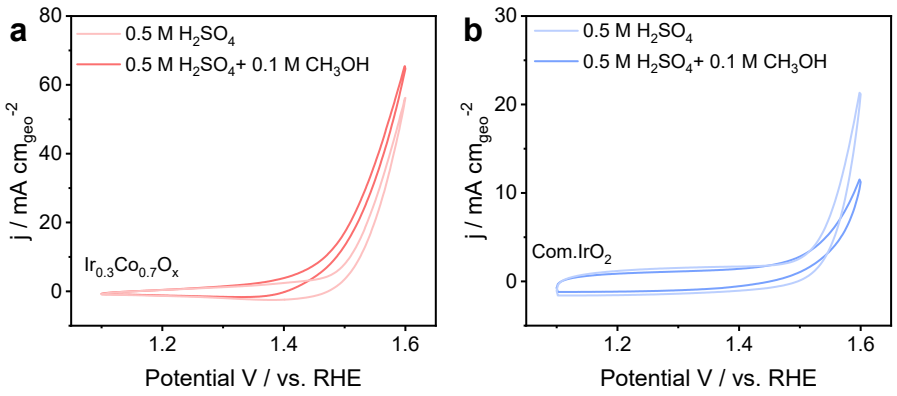

Fig. S38. Comparison of CV curves for (a) $Ir_{0.3}Co_{0.7}O_x$ and (b) $Com.IrO_2$ in 0.5 M H_2SO_4 and 0.5 M H_2SO_4 with 0.1 M CH_3OH.

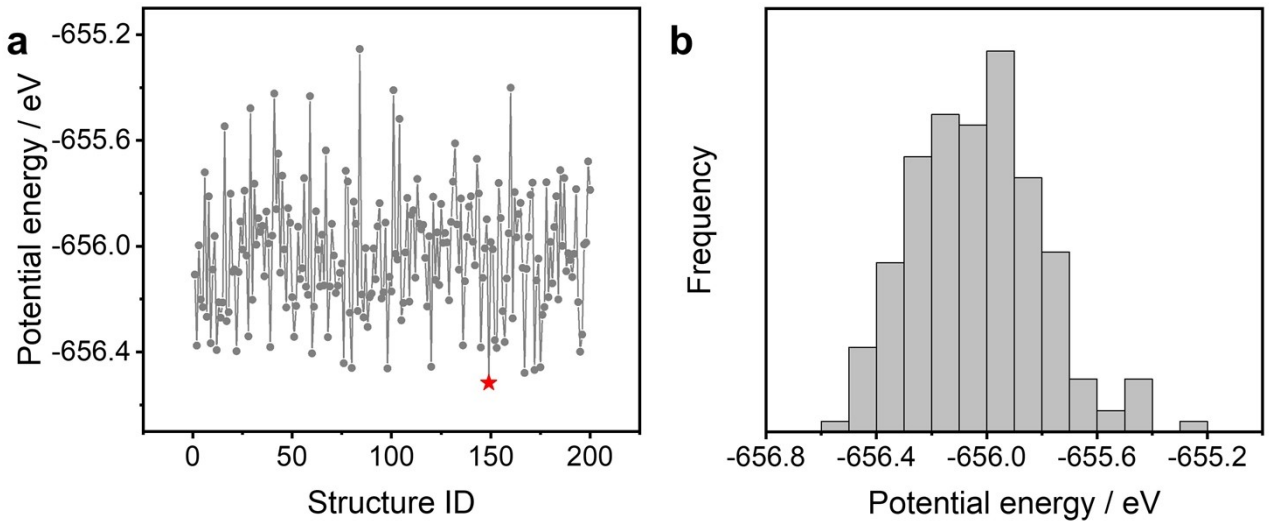

Fig. S39. The energy and distribution obtained from the optimization using a universal machine learning force field. (a) The energies of 200 randomly substituted structures after optimization with the universal machine learning force field, where the red star marks the lowest-energy structure, which is also the one used in subsequent calculations. (b) The frequency distribution histogram of the energies for these 200 structures.

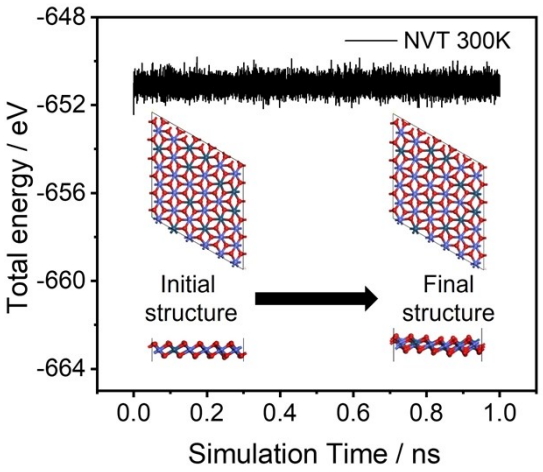

Fig. S40. The universal machine learning force field for the energy change of the 1ns NVT simulation, as well as the initial structure and the final structure after the 1ns simulation.

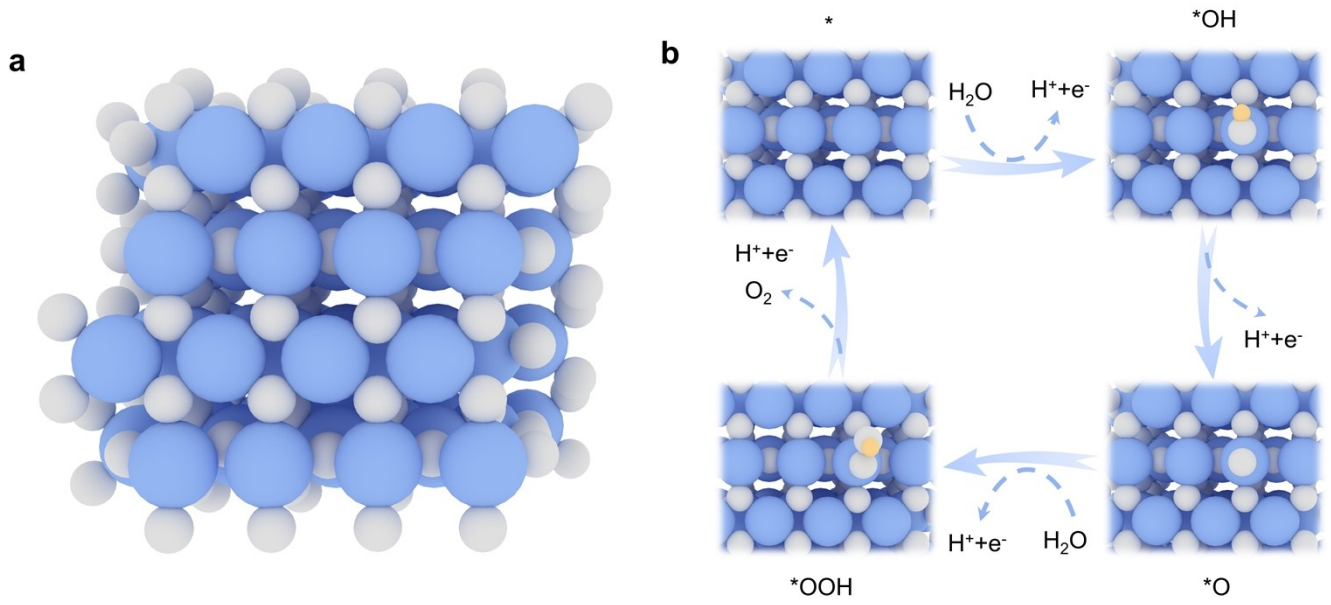

Fig. S41. (a) the top views of exposed (110) surface for Com.IrO_2. (b) Intermediate structure during OER of Com.IrO_2.

3. Supplementary Tables

Table S1. ICP-MS analysis of $Ir_{0.3}Co_{0.7}O_x$.

Catalyst	Ir content / wt %	Co content / wt %	Ir content / at %	Co content / at %
$Ir_{0.3}Co_{0.7}O_x$	59.46	40.54	31.04	68.96

Table S2. EXAFS fitting parameters at the Ir L_3-edge for $Ir_{0.3}Co_{0.7}O_x$, Com.IrO_2 and Ir foil.

Sample	Shell	[a]CN	[b]R / Å	[c]σ^2 / Å^2	[d]ΔE_0 / eV	*R*-factor
$Ir_{0.3}Co_{0.7}O_x$	Ir-O	5	2.006	0.003	5.8	0.02
	Ir-O-Co	4	2.556	0.008	11.595	0.02
	Ir-O-Ir	2	3.010	0.003	11.595	0.02
Com.IrO_2	Ir-O	6	1.973	0.001	10.648	0.004
Ir foil	Ir-Ir_1	12	2.703	0.001	8.491	0.007
	Ir-Ir_2	6	3.822	0.002	8.491	0.007

[a]CN, coordination number; [b]R, the distance between absorber and backscatter atoms; [c]σ_2, Debye-Waller factor to account for both thermal and structural disorders; [d]ΔE_0, inner potential correction; R factor indicates the goodness of the fit.

Table S3. Crystallographic information for $Ir_{0.3}Co_{0.7}O_x$.

Materials	Crystal system	Bravais lattice	Unit-cell dimensions	Space group
$Ir_{0.3}Co_{0.7}O_x$	Trigonal	Primitive	$a = b = 3.01$ Å, $c = 6.95$ Å; $\alpha = \beta = 90°$, $\gamma = 120°$	P-3m1 (164)

Table S4. The comparison of the OER performances of $Ir_{0.3}Co_{0.7}O_x$ and previously reported catalysts.

Electrocatalysts	Overpotential @ 10 mA cm^{-2} / mV	Tafel slope / mV dec^{-1}	Electrolyte	Reference
$Ir_{0.3}Co_{0.7}O_x$	235	50.8	0.5 M H_2SO_4	This work
IrCo@CNT/CC	241	92.2	0.5 M H_2SO_4	[7]
IrCoNi PHNC	303	53.8	0.1 M $HClO_4$	[8]
IrCo@NC-850	315	101	0.5 M H_2SO_4	[9]
IrCo-N-C	330	79	0.1 M $HClO_4$	[10]
IrCo@NCNT/PC	300	56	0.5 M H_2SO_4	[11]
IrCo NRAs	296.9	68.1	0.5 M H_2SO_4	[12]
Co-RuIr	235	66.9	0.1 M $HClO_4$	[13]
Co-IrCu ONC/C	293	50	0.1 M $HClO_4$	[14]
$Ir_1/Cu_{0.3}Co_{2.7}O_4$	290	71	0.1 M $HClO_4$	[15]
Co-IrRu/C	284	83	0.1 M $HClO_4$	[16]
Sr_2CoIrO_6	305	52	0.1 M $HClO_4$	[17]
$RuO_2/(Co,Mn)_3O_4$/CC	270	77	0.5 M H_2SO_4	[18]
FeCoNiIrRu/CNFs	241	153	0.5 M H_2SO_4	[19]
IrNi-RF	313.6	48.6	0.1 M $HClO_4$	[20]
IrNiCo	285	53	0.1 M $HClO_4$	[21]

Table S5. The comparison of the mass activities at 1.53 V vs. RHE for $Ir_{0.3}Co_{0.7}O_x$, Com.IrO_2, CoO_x and Co_3O_4.

Electrocatalysts	**Mass Activity@1.53 V vs. RHE**
$Ir_{0.3}Co_{0.7}O_x$	602.5 A g_{Ir}^{-1}
Com.IrO_2	13.5 A g_{Ir}^{-1}
CoO_x	4.4 A g_{Co}^{-1}
Co_3O_4	1.8 A g_{Co}^{-1}

Table S6. ICP-MS results after OER stability test for $Ir_{0.3}Co_{0.7}O_x$ catalyst.

Description	Co content / ppb	Co content / wt %	Ir content / ppb	Ir content / wt %
Stability test of $Ir_{0.3}Co_{0.7}O_x$ at 10 mA cm_{geo}^{-2} for 10 h	62	0.07	32	0.03
Stability test of $Ir_{0.3}Co_{0.7}O_x$ at 10 mA cm_{geo}^{-2} for 20 h	96	0.11	57	0.05
Stability test of $Ir_{0.3}Co_{0.7}O_x$ at 10 mA cm_{geo}^{-2} for 40 h	129	0.15	90	0.08

References

[1] J.P. Perdew, K. Burke, M. Ernzerhof, *Phys. Rev. Lett.*, 1996, **77**, 3865-3868.

[2] S. Grimme, S. Ehrlich, L. Goerigk, *J. Comput. Chem.*, 2011, 32, 1456-1465.

[3] S. Batzner, A. Musaelian, L.X. Sun, M. Geiger, J.P. Mailoa, M. Kornbluth, N. Molinari, T.E. Smidt, B. Kozinsky, *Nat. Commun.*, 2022, **13**, 2453.

[4] A.H. Larsen, J.J. Mortensen, J. Blomqvist, I.E. Castelli, R. Christensen, M. Dulak, J. Friis, M.N. Groves, B. Hammer, C. Hargus, E.D. Hermes, P.C. Jennings, P.B. Jensen, J. Kermode, J.R. Kitchin, E.L. Kolsbjerg, J. Kubal, K. Kaasbjerg, S. Lysgaard, J.B. Maronsson, T. Maxson, T. Olsen, L. Pastewka, A. Peterson, C. Rostgaard, J. Schiotz, O. Schütt, M. Strange, K.S. Thygesen, T. Vegge, L. Vilhelmsen, M. Walter, Z.H. Zeng, K.W. Jacobsen, *J. Phys. Condens. Matter*, 2017, **29**, 273002.

[5] Y. Park, J. Kim, S. Hwang, S. Han, *J. Chem. Theory Comput.*, 2024, 20, 4857-4868.

[6] D.C. Liu, J. Nocedal, On the limited memory bfgs method for large-scale optimization, *Math. Program.*, 1989, **45**, 503-528.

[7] X X. Wang, Z. Qin, J.J. Qian, L.Y. Chen, K. Shen, *ACS Catal.*, 2023, **13**, 10672-10682.

[8] J.R. Feng, F. Lv, W.Y. Zhang, P.H. Li, K. Wang, C. Yang, B. Wang, Y. Yang, J.H. Zhou, F. Lin, G.C. Wang, S.J. Guo, *Adv. Mater.*, 2017, **29**, 1703798.

[9] Y.Q. Zhou, L.F. Zhang, H.L. Suo, W.B. Hua, S. Indris, Y.J. Lei, W.H. Lai, Y.X. Wang, Z.P. Hu, H.K. Liu, S.L. Chou, S.X. Dou, *Adv. Funct. Mater.*, 2021, **31**, 2101797.

[10] M.L. Xiao, J.B. Zhu, S. Li, G.R. Li, W.W. Liu, Y.P. Deng, Z.Y. Bai, L. Ma, M. Feng, T.P. Wu, D. Su, J. Lu, A.P. Yu, Z.W. Chen, *ACS Catal.*, 2021, **11**, 8837-8846.

[11] D.K. Zhao, Y.G. Zhu, Q.K. Wu, W. Zhou, J.C. Dan, H. Zhu, W. Lei, L.J. Ma, L.G. Li, *Chem. Eng. J.*, 2022, **430**, 132825.

[12] Y. Zhang, G.L. Zhang, M.M. Zhang, X.J. Zhu, P.D. Shi, S.H. Wang, A.L. Wang, Chem. Eng. J., 2022, 433, 133577.

[13] J.Q. Shan, T. Ling, K. Davey, Y. Zheng, S.Z. Qiao, *Adv. Mater.*, 2019, **31**, 1900510.

[14] T. Kwon, H. Hwang, Y.J. Sa, J. Park, H. Baik, S.H. Joo, K. Lee, *Adv. Funct. Mater.*, 2017, **27**, 1604688.

[15] Z.R. Zhang, C.Y. Jia, P.Y. Ma, C. Feng, J. Yang, J.M. Huang, J.N. Zheng, M. Zuo, M.K. Liu, S.M. Zhou, J. Zeng, *Nat. Commun.*, 2024, **25**, 1767.

[16] Y. Li, L. Zhao, X. Du, W.T. Gao, C. Zhang, H. Chen, X. He, C. Wang, Z.Q. Mao, *Chem. Eng. J.*, 2023, **461**, 141823.

[17] Y.Y. Pu, Y.F. Liu, X.S. Tang, Q. Huang, L.M. Huang, *Appl. Catal. B Environ.*, 2024, **341**, 123319.

[18] S.Q. Niu, X.P. Kong, S.W. Li, Y.Y. Zhang, J. Wu, W.W. Zhao, P. Xu, *Appl. Catal. B Environ.*, 2021, **297**, 120442.

[19] H. Zhu, Z.F. Zhu, J.C. Hao, S.H. Sun, S.L. Lu, C. Wang, P.M. Ma, W.F. Dong, M.L. Du, *Chem. Eng. J.*, 2022, **431**, 133251.

[20] H. Jin, Y. Hong, J. Yoon, A. Oh, N.K. Chaudhari, H. Baik, S.H. Joo, K. Lee, *Nano Energy*, 2017, **42**, 17-25.

[21] W.Q. Zaman, Z.Q. Wang, W. Sun, Z.H. Zhou, M. Tariq, L.M. Cao, X.Q. Gong, J. Yang, *ACS Energy Lett.*, 2017, **2**, 2786-2793.